Spectrochimica Acta Part B 66 (2011) 421–431

Contents lists available at ScienceDirect

Spectrochimica Acta Part B

journal homepage: www.elsevier.com/locate/sab

Multi-element model for the simulation of inductively coupled plasmas: Effects of helium addition to the central gas stream

Helmut Lindner *, Annemie Bogaerts

PLASMANT-Plasma, Laser ablation & Surface Modelling Antwerp, Department of Chemistry, University of Antwerp, Universiteitsplein 1, 2610 Antwerpen, Belgium

ARTICLE INFO

Article history:
Received 22 December 2010
Accepted 7 April 2011
Available online 14 April 2011

Keywords:
Argon ICP simulation
Helium addition
Multi-element
Element analysis
Atmospheric pressure plasma

ABSTRACT

A model for an atmospheric pressure inductively coupled plasma (ICP) is developed which allows rather easy extension to a variable number of species and ionisation degrees. This encompasses an easy calculation of transport parameters for mixtures, ionisation and heat capacity. The ICP is modeled in an axisymmetric geometry, taking into account the gas streaming into a flowing ambient gas. A mixture of argon and helium is applied in the injector gas stream as it is often done in laser ablation ICP spectrometry. The results show a strong influence of the added helium on the center of the ICP, which is important for chemical analysis. The length of the central channel is significantly increased and the temperature inside is significantly higher than in the case of pure argon. This means that higher gas volume flow rates can be applied by addition of helium compared to the use of pure argon. This has the advantage that the gas velocity in the transport system towards the ICP can be increased, which allows shorter washout-times. Consequently, shorter measurement times can be achieved, e.g. for spatial mapping analyses in laser ablation ICP spectrometry. Furthermore, the higher temperature and the longer effective plasma length will increase the maximum size of droplets or particles injected into the ICP that are completely evaporated at the detection site. Thus, we expect an increase of the analytical performance of the ICP by helium addition to the injector gas.

1. Introduction

Inductively coupled plasmas (ICP) at atmosperic pressure are widely used for chemical analysis, in combination with various types of mass spectrometric (MS) or optical emission spectrometric (OES) detection systems. They provide a very high sensitivity so that very low concentrations of analyte can be determined. ICP spectrometry is a mature technique which is 30 years old in the case of the coupling with MS [1] and even older for the coupling with OES [2,3].

Nevertheless, the ICP still requires better understanding and improvement for certain applications. Recently, ICPs have been used for the characterisation of single nano-particles [4]. This is a crucial application for environmental analysis (particulate matter) and also because more and more nano-particles are produced for various applications in industry or medicine and hence, need to be analysed as well. Furthermore, new sample introduction systems are under investigation to apply minimal amounts of analyte at high efficiency to the ICP [5,6]. Another approach for further improvement of ICPs is to use new kinds of torches which only require a small amount of argon compared to usual torches [7–9].

Additionally, the effects of injecting many different species (e.g. pure water droplets already add atomic and molecular oxygen, hydrogen, water vapour, etc. to the plasma) into the ICP is not yet fully understood. Indeed, there are many interactions and dependences going on in such a complex plasma, see e.g. [10,11]. Thus, it is of crucial importance that ICPs can be modeled for various kinds of mixtures.

All these different fields of applications require better understanding of the processes going on inside the plasma. The present paper provides a step towards a more easy simulation of such mixture plasmas. Furthermore, the present approach will allow a rather easy way to analyze different torch geometries.

ICPs were already widely simulated for (a) 'closed' torches, i.e. the torch went through the whole calculation region and (b) a pure plasma composition of argon [12], helium [13] or nitrogen [14]. Approaches for mixed plasmas are given in [15,16]. The main focus of previous investigations was on effects of e.g. variation of coil geometry [17] or improved electric field treatment [18]. These plasmas were simulated for other applications than chemical analysis, e.g. high power ICPs for waste treatment [19,20]. The simulations often apply transport parameters (e.g. viscosity) from the literature. This, however, limits the applicability to mixtures where the data for exactly that mixture (species and relative concentrations) is known. Especially the ionisation degree is dependent on the actual composition of the plasma which has strong effects on the transport parameters.

* Corresponding author. Tel.: +32 3 265 2383; fax: +32 3 265 2376.
E-mail address: helmut.lindner@ua.ac.be (H. Lindner).

0584-8547/$ – see front matter © 2011 Elsevier B.V. All rights reserved.
doi:10.1016/j.sab.2011.04.007

In the present work, only data from pure species (i.e. argon and helium) are taken from literature and the resulting transport parameters for the mixtures are calculated in a kinetic model. This makes it possible to apply the model to a wider variety of gas mixtures.

In the first part of the paper, the geometry and basic simulation setup conditions are presented and subsequently the model is explained. After that, simulation results of an argon ICP will be presented with the addition of different ratios of helium to the injector gas. Finally, a conclusion will be given.

2. Simulation setup

For the calculations, the commercial computational fluid dynamics (CFD) program Fluent v12.1 (ANSYS) was used. The SIMPLE algorithm was employed as solver in the simulation. Some self-written modules were added as user defined functions (UDFs) for the parts relevant for the plasma and the material parameters. The electric fields were solved as user defined scalars (UDSs) in Fluent. The 2 d axisymmetric geometry of the setup is displayed in Fig. 1 and the important data are presented in Table 1. The figure of the torch is in scale, however, not the whole calculation region is shown. Indeed, the calculation region had an axial length of 15 cm and a radius of 10 cm. The geometry was subdivided into about 23,000 cells of which about half are located inside and directly behind the torch. The gas coming through the three concentric tubes of the ICP-torch flows into an open ambient gas which was taken to be argon for simplicity. The volume flow rate through the outer torch tube (plasma gas) and through the intermediate torch tube (auxilliary gas) were fixed at 16 L/min and 1 L/min, respectively. The central gas flow rate was set to 0.7 L/min. The flow rate of the ambient gas was determined by the pressure difference between the ambient pressure (101325 Pa) and the pressure set for the exhaust (101225 Pa). The flow was treated to be laminar. The flow conditions are also displayed in Table 1.

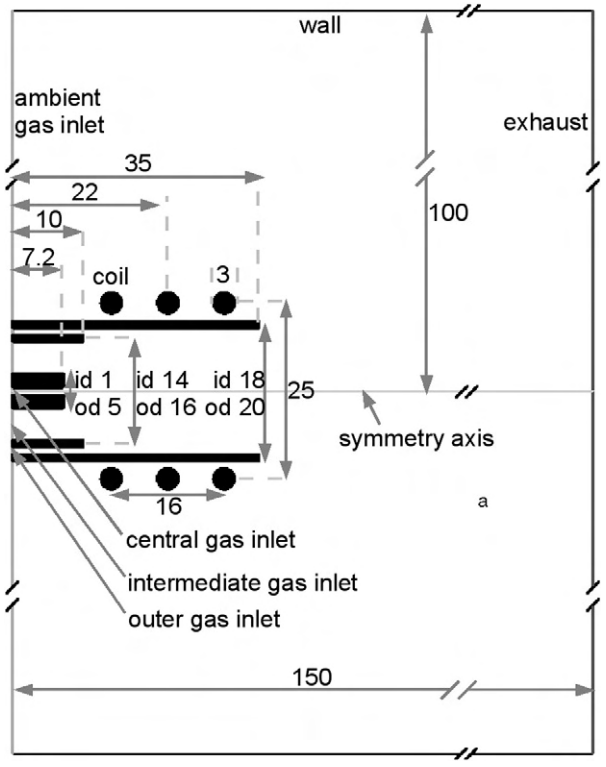

Fig. 1. Geometry used for the simulation. The calculation region was mirrored at the symmetry axis for better readability. The data are given in mm. The geometry of the torch is in scale while the distances of the borders were reduced for better readability.

Table 1
Operating conditions for the ICP.

Frequency	27 MHz
Coupled power	1000 W
Central gas flow rate	Ar + He; 0.7 L/min
Intermediate gas flow rate	Ar; 1 L/min
Outer gas flow rate	Ar; 16 L/min
Ambient pressure	101325 Pa
Exhaust pressure	101225 Pa
Number of coil turns	3
Coil diameter	25 mm
Distance of two coil turns	8 mm
Coil wire diameter	3 mm
Injector diameter	1 mm

The applied geometry automatically makes use of the 'extended' electric field modeling as it was described in [18] which allows the use of simpler electric field boundary conditions. The electric field was assumed to be zero at the border of the calculation region. This can be regarded as the equivalent of the metal shielding box around the ICP which prevents the rf radiation from entering the laboratory.

The model assumes local thermodynamic equilibrium (LTE). All equations presented in this manuscript make explicitly or implicitly use of this assumption. The plasma is burning at atmospheric pressure. Thus, collision times are in the order of 10 ps while one period of the rf-field takes a few ten ns. Thus, in the order of 1000 collisions with atoms take place per electron during one oscillation. In contrast to DC discharges, electrons do not gain energy on average if they do not undergo collisions since the oscillating electric field accelerates and decelerates them in the same way during one period. This means that close-to LTE conditions can be achieved. Although the assumption of LTE is not fully correct, the use of two-temperature models does not necessarily yield significantly different temperatures for electrons and heavy species [21]. Therefore, we believe that the assumption of LTE can get close to the accuracy of non-LTE models for the present plasma. LTE, in particular, has the advantage that the model can be more easily formulated consistently and it requires less other assumptions (e.g. on power coupling and energy transfer from electrons to atoms and ions) and/or (sometimes imprecise) parameters.

3. Theoretical background

3.1. Flow field and power coupling

The flow in the calculation region is assumed to be laminar. Thus, the well-known Navier-Stokes equations [22] are used to determine the flow conditions. Source terms taken into account for the momentum equation are the pressure gradient originating from the electron distribution and the Lorentz force. The viscosity (see below) was defined in a UDF. The time-averaged Lorentz force density is calculated from

$$\langle f_{Lr} \rangle = \frac{1}{2}\sigma\left(E_{1\phi}B_{1z} + E_{2\phi}B_{2z}\right) \quad (1)$$

$$\langle f_{Lz} \rangle = -\frac{1}{2}\sigma\left(E_{1\phi}B_{1r} + E_{2\phi}B_{2r}\right) \quad (2)$$

where the symbols are defined in the appendix.

The energy equation of Fluent v12.1 was used for the power coupling (see [22]). Two source terms are added to the energy equation: the coupled electric power density and the energy loss by emitted radiation (see Section 3.2). The heat capacity and the thermal conductivity (see below) were defined as UDFs.

The time-averaged power density p was coupled into the plasma by the simple Ohm's law

$$<p> = <\vec{j}\,\vec{E}> = \frac{1}{2}\sigma\left(E_{1\phi}^2 + E_{2\phi}^2\right) \quad (3)$$

The total power coupled to the plasma was set to 1000 W. To achieve this value, the external current I_{ext} (and subsequently the electric fields) were adapted accordingly during the iterations. Such an adaption can roughly be regarded as the equivalent of an electric oscillating circuit that keeps the plasma running in reality [23].

3.2. Radiation

For the calculation of the radiation, the following formula was used [24]

$$p_{rad} = 4\pi\left(n_e^2\cdot\left(C_1 + \frac{C_2}{T^{0.5}} + \frac{C_3}{T} + C_4\cdot T + C_5\cdot T^{1.5}\right)\cdot exp\left(\frac{C_6}{T}\right)\right) \quad (4)$$

The unit of p_{rad} is W/m^3 and the temperature is to be taken in K, the electron density is in m^{-3} and the parameters are $C_1 = -6.932\cdot 10^{-41}$, $C_2 = 4.753\cdot 10^{-39}$, $C_3 = -5.808\cdot 10^{-38}$, $C_4 = -2.843\cdot 10^{-45}$, $C_5 = 8.629\cdot 10^{-47}$, $C_6 = 6.706\cdot 10^4$. It was assumed that the plasma is optically thin, so that no absorption or scattering inside the plasma was taken into account. Although the radiation emission from [24] is in principle only valid for argon, the approximation is still reasonable for the present case: indeed, the main contribution of energy loss is due to continuous radiation, namely free-free and free-bound transitions of the electrons [25]. The ionisation potential of helium is high compared to argon and thus, not many helium ions are present. They would be needed to cause significant background radiation. Hence, even though helium molefractions of up to about 25% can be present in the hot plasma regions (see below) they should not modify the emitted radiative power too much.

3.3. Electro-magnetic fields

The external electric current density (i.e. current density inside the induction coil) was chosen to be harmonic in the following form

$$\vec{j}_{ext} = \vec{j}_{ext0}sin(\omega t) \quad (5)$$

where the direction of the current is in the angular direction (ϕ-direction) of the cylindric coordinate system. The total electric field in the angular direction $\vec{E}_\phi$ is assumed to be

$$\vec{E}_\phi = \vec{E}_{1\phi}cos(\omega t) + \vec{E}_{2\phi}sin(\omega t) \quad (6)$$

Due to the symmetry of the present geometry, no other directions of the electric field need to be taken into account. Then, the amplitudes of the electric fields can be calculated from the equations

$$\Delta E_{1\phi} = \mu_0\omega j_{ext0} + \mu_0\omega\sigma E_{2\phi} + \frac{E_{1\phi}}{r^2} \quad (7)$$

$$\Delta E_{2\phi} = -\mu_0\omega\sigma E_{1\phi} + \frac{E_{2\phi}}{r^2} \quad (8)$$

The Laplace operators given in Eqs. (7) and (8) are treated as being applied on scalars (i.e., as mentioned above, the electric fields are solved in Fluent as UDS). Therefore, the contribution of applying the Laplace operator on a vector in cylindrical coordinates is taken into account by the addition of the E_i/r^2 term on the right hand sides of Eqs. (7) and (8). Assumptions made in the derivation from the Maxwell equations are vanishing divergence of the electric field, negligible displacement current, μ_r equal to one and time-independent electric conductivity. Note that for the latter assumption it is sufficient that a temporal change is slow compared to the oscillation time of the electro-magnetic fields. The Eq. (7) and (8) are equivalent to the commonly used vector potential formulation, see for instance [18,26].

The magnetic fields were calculated from the respective spatial derivatives of the electric fields given by

$$B_{1r} = -\frac{1}{\omega}\frac{\partial E_{2\phi}}{\partial z} \quad (9)$$

$$B_{1z} = \frac{1}{\omega}\left(\frac{E_{2\phi}}{r} + \frac{\partial E_{2\phi}}{\partial r}\right) \quad (10)$$

$$B_{2r} = +\frac{1}{\omega}\frac{\partial E_{1\phi}}{\partial z} \quad (11)$$

$$B_{2z} = -\frac{1}{\omega}\left(\frac{E_{1\phi}}{r} + \frac{\partial E_{1\phi}}{\partial r}\right) \quad (12)$$

3.4. Material parameters

3.4.1. Viscosity

The viscosity of the mixture consisting of the species denoted by k (heavy species and electrons) was calculated from the generalisation of the pure element viscosity equation [27]

$$\eta = \sum_k \sqrt{\frac{k_B T}{\pi}}\frac{n_k\cdot m_k}{\sum_i \sqrt{\mu_{ki}}n_i S_{ki}} = \eta_e + \sum_{k\neq e}\eta_k \quad (13)$$

where m_k is the mass of the species k and μ_{ki} is the reduced mass of the species k and i. The pre-factor 0.499 given in [27] was treated as 0.5 because the accuracy is worse than 0.2%, anyway. The square-root in the denominator originates from the different relative velocities of different species at the same temperature T. The viscosity of the electrons is also taken into account but it is effectively negligible due to the small mass of the electrons.

The cross-sections for neutral-neutral and neutral-charged collisions were calculated from

$$S_{ki} = \sqrt{2}\pi\left(R_{eff,k} + R_{eff,i}\right)^2 \quad (14)$$

where the radius of electrons was neglected here. The temperature dependent diameters for helium and argon were calculated from the data of the pure elements given in [27–29]. The fit functions used during the calculation are given in Table 2. The collision cross-section for charged particles was taken as [30]

$$S_{ki} = Z_k^2 Z_i^2\cdot 3\pi b_0^2\left(ln\Lambda_C + \frac{1}{2}ln\left(\frac{3\pi}{2}\right)\right) \quad (15)$$

where $ln\Lambda_C = 12\pi\lambda_D^3 n_e$ is the Coulomb logarithm and $b_0 = e^2/(12\pi\varepsilon_0 k_B T)$ is the 90-degree collision parameter.

3.4.2. Thermal conductivity

For monoatomic species, the thermal conductivity can be expressed as [31]

$$k = \frac{15}{4}\cdot\frac{k_B}{m_e}\eta_e + \sum_k\sum_{Z_k}\frac{15}{4}\cdot\frac{k_B}{m_k}\eta_{k,Z_k} \quad (16)$$

In contrast to the viscosity, small masses have a strong influence on the thermal conductivity. Consequently, the first term, originating from the electrons, gives a strong contribution if a sufficient number of free electrons is present. This can be seen in the effective diameter

Table 2
Fit functions used for the calculation of the effective diameter of argon and helium; the temperature is in K; the parameters are derived from viscosity data given in [27–29].

Element	Effective diameter [m]	Temperature range
Ar	$d = \frac{5.2603\cdot10^{-10}}{(T-154.46485)^{0.0825}} - 7.0465\cdot10^{-16}\cdot T + 1.2167\cdot10^{-11}$	273 K<T<9300 K
	$d = 3.3\cdot10^{-28}\cdot(T-7700)^{4.7} + 2.5275\cdot10^{-10}$	9300 K≤T<12000 K
He	$d = \frac{9.5066\cdot10^{-6}}{(T+1133.33407)^{1.66528}} - 2.6575\cdot10^{-15}\cdot T + 1.6499\cdot10^{-10}$	273 K<T<11250 K

graph (Fig. 2), where the effective diameter becomes abruptly smaller at a temperature of somewhat less than 7000 K. Consequently it is better to determine the effective atomic radius from viscosity data rather than from thermal conductivity data, at least for higher temperatures. Note that even then the ionic diameter (for interactions with neutrals) should not deviate too much from the atomic one.

In Fig. 3 the thermal conductivities calculated with Eq. (16) are compared with the values given by [27–29]. The data are in good agreement (typically less than 5% deviation) for both the pure elements as well as for the example mixture of 50% He and 50% Ar (mole fraction). The maximum deviations reach values of about 10%, which is similar to deviations of the data given in e.g. [32] with respect to [29]. The deviations appear in the range where significant ionisation is present.

3.4.3. Heat capacity

The heat capacity contribution of ionisation can be calculated from

$$c_{p,ion} = \left.\frac{\partial H_{ion}}{\partial T}\right|_p \tag{17}$$

The enthalpy originating from ionisation can be calculated from

$$H_{ion} = \sum_k \frac{N_A}{M_{Hges}} x_{Hk} \sum_{Z=1}^{Z_{max,k}} \left(\sum_{l=1}^{Z} E^{eff}_{ion,kl} \right) x_{kZ} + \frac{N_A}{M_{Hges}} Z_{av} \frac{5}{2} k_B T \tag{18}$$

$E^{eff}_{ion,\,kl}$ is the ionisation potential of the ionisation level l of element k, corrected for the ionisation potential reduction (see Eq. (23)). The last term in Eq. (18) accounts for the heat capacity c_{pe} of free electrons. The mean molar mass M_{Hges} is calculated from

$$M_{Hges} = \sum_k x_{Hk} M_k \tag{19}$$

where x_{Hk} are the molar fractions of the elements ($x_{Hk} = n_{Hk}/n_{Hges}$). Fluent v12.1 only provides temperature and mass fractions of the elements for the c_p calculation. Therefore, a constant heavy particle pressure of 101,225 Pa was assumed within the whole calculation region from which the total heavy particle number density and subsequently the c_p contribution of ionisation was calculated. This assumption introduces only a small error in the present case since the pressure does not deviate much from that value throughout the calculation region.

3.4.4. Diffusion

The isotropic diffusion coefficients [31] for the elements k are taken into account in the present model by,

$$D_k = \frac{6}{5} \sum_{Z=1}^{Z_{max,k}} x_{kZ} \sqrt{\frac{k_B T}{\pi}} \frac{1}{\sum_i \sqrt{\mu_{ki}} n_i S_{ki}} \tag{20}$$

where $x_{kZ} = n_{kZ}/n_{Hk}$. Ambipolar diffusion [33] was not applied since it would require asymmetric diffusion coefficients for the multi-component plasma within the framework of the present model. The ambipolar diffusion is only relevant for ionic species. For plasmas containing only three species (i.e. atoms, singly charged ions and electrons), the diffusion coefficient of the ions doubles [33]. The maximum ionisation degree for the present conditions is less than 3%. The possible error from this effect on diffusion can hence be estimated to be below 3%. We expect that this error lies within the uncertainty of our model.

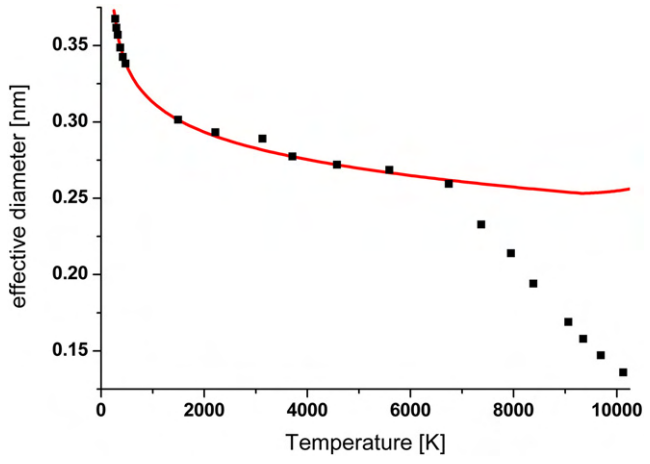

Fig. 2. Effective diameter of argon used in the calculations (continuous line; determined from viscosity) and effective diameter calculated from thermal conductivity (black squares); the viscosity and thermal conductivity data are taken from [27,28].

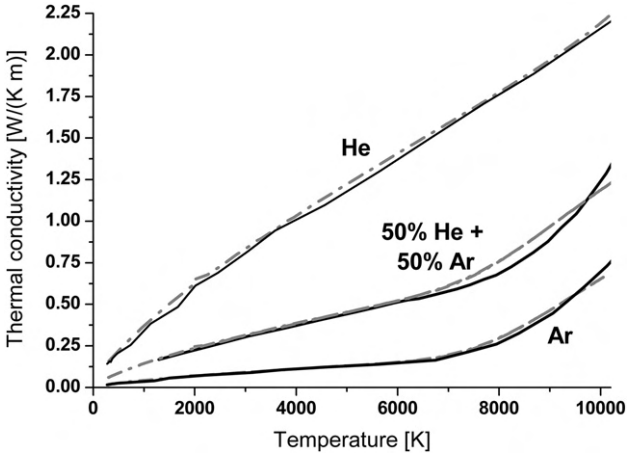

Fig. 3. Thermal conductivity for pure argon (bottom lines), a mixture of 50% argon and 50% helium mole fractions (intermediate lines) and pure helium (top lines) — comparison between the used values (gray, dash-dotted) and literature data (black, solid) [27–29].

3.5. Ionisation

The ionisation was treated for local thermodynamic equilibrium (LTE), i.e. the Saha-equation

$$\frac{n_e n_{k,Z}}{n_{k,Z-1}} = 2\frac{\zeta_{k,Z}}{\zeta_{k,Z-1}}\left(\frac{2\pi m_e k_B T}{h^2}\right)^{3/2} exp\left(-\frac{E_{ion,k,Z}-\Delta E_{ion}}{k_B T}\right) = : K_{k,Z} \quad (21)$$

was applied. Furthermore, quasi-neutrality and conservation of heavy particles of each element are assumed. The sum of all heavy particle number densities gives the total heavy particle number density n_{Hges}. The electron density can be written as the product of average ionisation degree Z_{av} and n_{Hges}.

The derivation to calculate the average ionisation degree Z_{av} followed basically the derivation given in [34], except that the 'heavy particle fractions' were inserted into the quasi-neutrality equation for more than one element. In this way, only one transcendent equation needs to be solved for any number of elements and any number of ionisation stages, as is also presented in [35]. The equation to be solved is

$$Z_{av} = \sum_k x_{Hk}\left[\frac{\sum_{Z=1}^{Z_{max,k}} Z\frac{\prod_{j=1}^{Z} K_{k,j}}{\left(n_{Hges}Z_{av}\right)^Z}}{1+\sum_{Z=1}^{Z_{max,k}}\frac{\prod_{j=1}^{Z} K_{k,j}}{\left(n_{Hges}Z_{av}\right)^Z}}\right] \quad (22)$$

where $K_{k,\,Z}$ means the right hand side of the Saha-equation of the different species (see Eq. (21)) and $x_{Hk} = n_{Hk}/n_{Hges}$.

The ionisation potential reduction was calculated from [35]

$$\Delta E_{ion} = \frac{Ze^2}{4\pi\varepsilon_0(\lambda_D + \lambda_B/8)} \quad (23)$$

where λ_D is the Debye-length taken as

$$\lambda_D = \sqrt{\frac{\varepsilon_0 k_B T}{e^2}\left(n_e + \sum_k \sum_{Z=1}^{Z_{max,k}} Z^2 n_{kZ}\right)} \quad (24)$$

and where the de Broglie length λ_B is

$$\lambda_B = \sqrt{\frac{h^2}{2\pi m_e k_B T}} \quad (25)$$

The partition functions of argon were calculated according to the functions given in [36]. For temperatures below 1000 K, the value was kept the same as for 1000 K which has no influence since ionisation is negligible in that temperature range. The partition functions of helium are constant in the temperature range under study and have values of 1 for atomic helium and 2 for He^+. Heavy species taken into account in the calculations are Ar, Ar^+, Ar^{2+} and He, He^+.

4. Results and discussion

In analytical chemistry, an analyte is injected into the plasma as particles or droplets through the central gas stream ("injector gas stream"). For a plasma arrangement as in the present study, optical emission would be used for the detection of the analyte. In "side-on" detection, the radiation is collected from a small region shortly behind the torch. Since the analyte is – or should be – present mainly in the central part of the plasma, we take a closer look at this part. The detection point is typically several mm above the load coil (height above load coil, HALC). This means that effects on the droplets or particles taking place in the plasma behind that position do not have an effect on the detection of the analyte. On the other hand, the analyte needs to be in the gas phase to be detectable. Thus, the droplet or the particle needs to be evaporated completely at the point of detection to allow proper determination of the analyte. This is, however, strongly dependent on the path followed by the droplet or particle through the plasma and especially on whether it remained sufficiently long in a hot region. In the following, the effect of different He/Ar mole fractions in the injector gas on several plasma characteristics will be investigated.

4.1. Temperature distribution

Fig. 4 shows the temperature distribution in and around the torch for pure argon, pure helium and a mixture of 50% argon and 50% helium (mole fractions) as central gas. Inside the torch, the gas sheet next to the torch wall stays cool due to the strong outer gas stream of 16 L/min (see Table 1). At the connection to the ambient gas, the plasma widens somewhat but does not enter very deep into the ambient gas zone. The extend of the plasma is similar for the three cases and applies also for the other He/Ar mole fractions investigated.

The hottest region of the plasma in the radial direction is close to the middle of the intermediate gas inlet. In the axial direction, the start of the highest temperature region shifts to higher axial positions with increasing He/Ar fraction in the central gas, from the end of the first coil turn for pure argon to the middle of the second coil turn for pure helium.

However, the most significant changes between the different cases occur in the central part of the plasma. In the case of pure argon (Fig. 4a) a clear central channel is formed, i.e. there is a colder central region surrounded by a hotter region. For the 50/50-mixture case (see Fig. 4b), a central channel exists but it is less pronounced than for pure argon. In the case of pure helium as injector gas (Fig. 4c) there is no central channel visible.

To investigate this effect in more detail, Fig. 5 displays the temperature along the symmetry-axis for different He/Ar fractions. The temperature rises quickly to a maximum value and drops slowly with axial position. The steepness of the temperature rise becomes more pronounced with higher He/Ar fractions. The crosses in the figure denote the position where a temperature of 3000 K is reached which we define as the "start of the plasma". With rising He/Ar fraction this start shifts towards earlier positions on the axis. Furthermore, the maximum temperature also increases with increasing He/Ar fraction in the central gas. At higher positions on the axis, the curves approach each other and exhibit nearly the same behaviour, although the temperature drops slightly quicker with higher He/Ar fractions. Thus, the central region of the plasma is dominated by the central gas for the first few centimeters while it is rather independent of it later on.

In Fig. 6, the maximum temperature on the axis is displayed vs. the He mole fraction inside the central gas. The temperature rises nearly linearly until a He mole fraction of about 80% and then it approaches a constant value of 10,300 K afterwards. The change in maximum temperature between no helium addition and pure helium in the central gas reaches about 1350 K. The linear temperature rise up to 70% He mole fraction can be fitted in the present case by $T = 16.9[K/\%]\cdot\%He + 8960[K]$. This indicates that a rather easy adjustability of the temperature at fixed volume flow rate is possible. It is, however, probable that this dependence is only applicable and of relevance for relatively high volume flow rates (for the pure argon case) where the central part of the plasma is significantly cooled compared to the border of the plasma. This, however, needs to be analysed in detail and is beyond the scope of this paper.

It is important to know the plasma conditions at the point of detection. Therefore, the temperature at a HALC of 10 mm is shown in Fig. 7. Here, the temperature rises linearly with the He mole fraction,

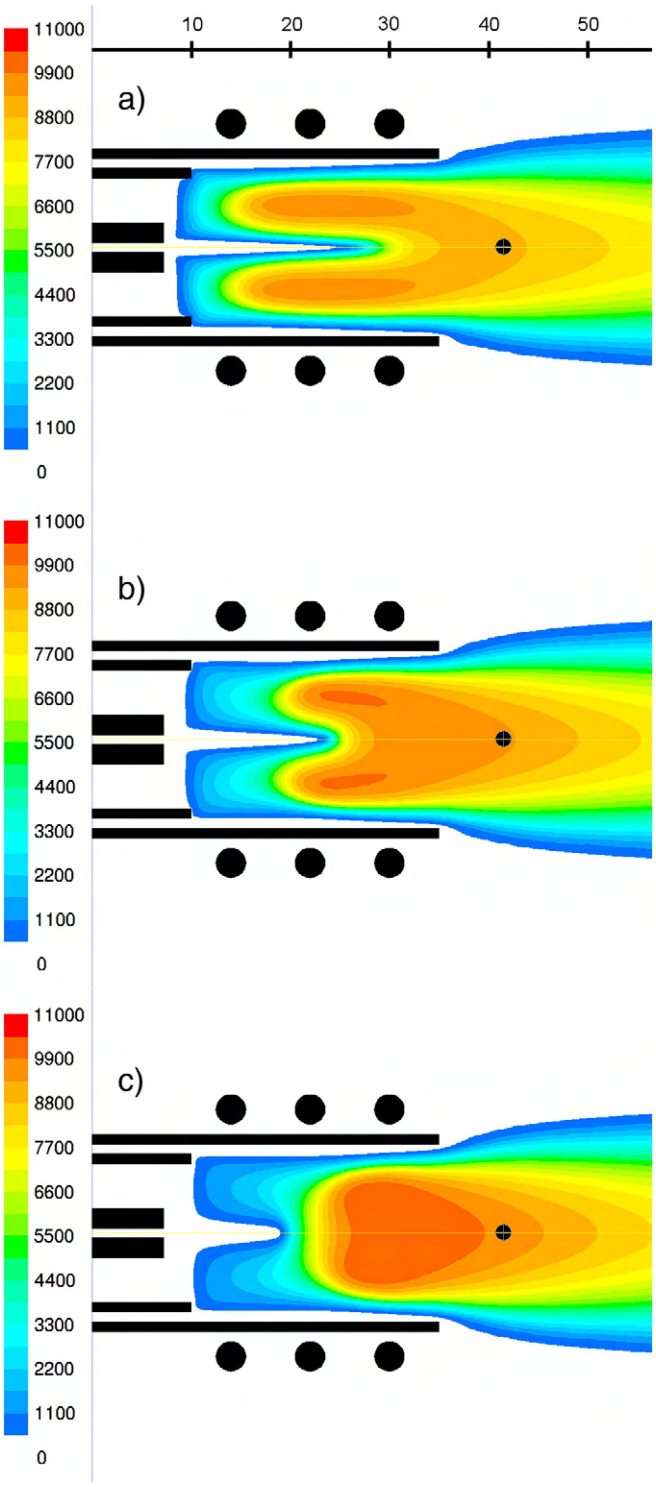

Fig. 4. Temperature (in K) distribution for a) 100% argon, b) 50% argon and 50% helium (mole fractions) and c) 100% helium as injector gas. The injector gas flow rate was 0.70 L/min. The black dot on the axis denotes the detection position at a HALC of 10 mm. The length scale is in mm and the 0 mm-position denotes the left border of the calculation region. Distances in axial and radial direction have the same scale.

too (cf. Fig. 6). The temperature difference between the cases of a helium mole fraction of 70% and pure argon and is about 800 K. Thus, the temperature is still significantly higher at the detection point with helium addition. This will result in a stronger excitation of the analyte at the point of detection which could improve the sensitivity. Note

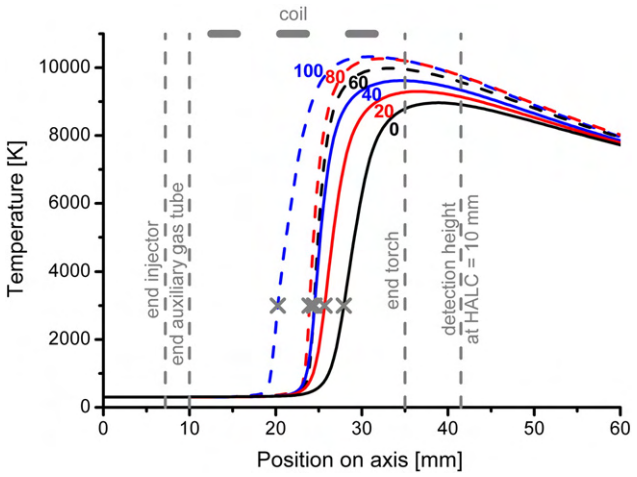

Fig. 5. Temperature along the symmetry axis for different He/Ar mole fractions in the central gas; the crosses display the position where the temperature of 3000 K is reached; the first vertical line denotes the end of the injector tube, the second one denotes the end of the torch, and the third one denotes an assumed detection height at HALC of 10 mm; the labels denote the%-Helium mole fractions.

that the extent of the temperature difference is dependent on the position of detection. The temperature difference will be higher for smaller HALCs as detection positions, and it will be smaller for higher HALCs, cf. Fig. 5. For very far positions (further than displayed in Fig. 5), the temperature for high He-content will even be lower than for low He-content in the central gas. Note that the actual behaviour will of course be dependent on the ambient gas.

4.2. Effective plasma length

The effective plasma length is shown in Fig. 8. We defined the effective plasma length as the distance between the position where the plasma temperature exceeds 3000 K (see above and Fig. 5) on the axis and the point of detection, chosen to be at 10 mm HALC. The effective plasma length rises nearly linearly until a He/Ar mole fraction of 30%. After that, the plasma length keeps nearly constant up to a He-fraction of 70%. Subsequently, it increases further. The plasma

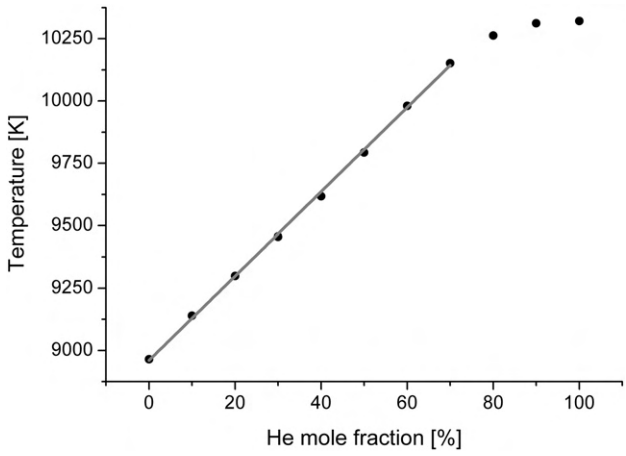

Fig. 6. Maximum temperature on the axis in dependence on the helium mole fraction in the central gas.

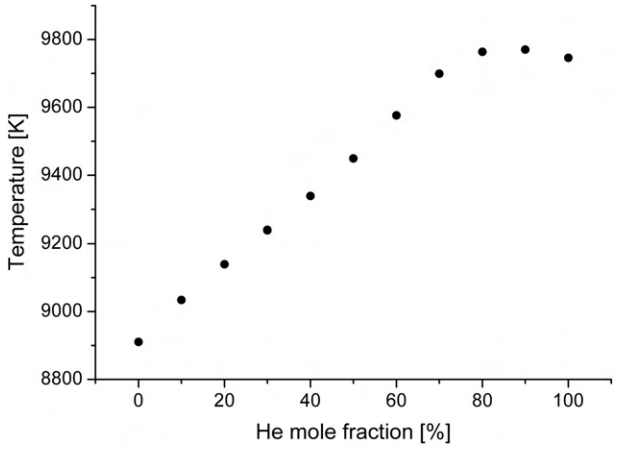

Fig. 7. Temperature at the detection position of HALC = 10 mm on the axis in dependence on the helium mole fraction in the central gas.

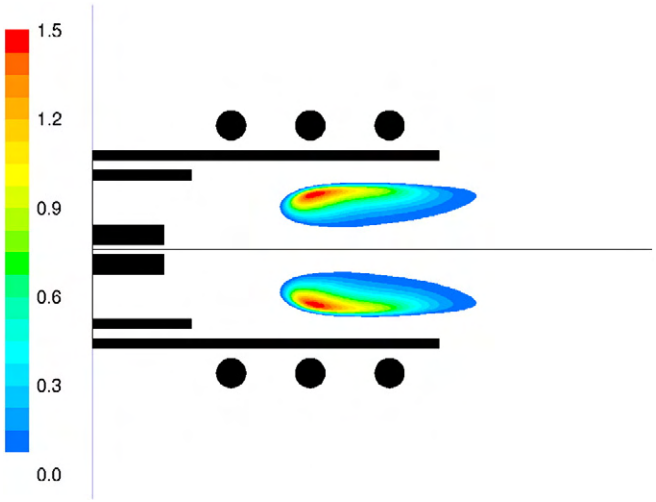

Fig. 9. Coupled power density (in GW/m^3) for 50% Ar and 50% He as injector gas at a flow rate of 0.70 L/min.

length increases by 25% for a helium fraction of the plateau region compared to pure argon. If the detection position was at a lower position, the relative change would be even more pronounced. Thus, the droplets or particles can pass through a larger high temperature region, and hence, they have more chance to become fully evaporated, if helium is added to the central gas stream.

4.3. Power coupling into the plasma

The effect of increased temperature and longer plasma length in the case of higher He fraction can be explained in the following way: the power is coupled into the borders of the plasma which is illustrated for the 50/50-mixture case in Fig. 9. The qualitative picture is the same for the different He-contents inside the central gas, even for 100% He. This is a result from the fact that the electric field is strong at the outer border of the torch and zero in the center. Thus, although there is a high electric conductivity present in the central part for e.g. pure helium as central gas, not much power is coupled into these regions. Therefore, the energy coupled to the outer borders of the plasma needs to be transported towards the center to heat it up. As can be seen in Fig. 3, the thermal conductivity of helium and helium-argon mixtures is much larger than that of pure argon. Thus, much more energy is transported to the plasma core when helium is applied in the central gas.

Furthermore, for higher helium concentration in the central gas the outer borders of the plasma become shorter, i.e. the volume where the power is coupled into becomes smaller. In order to keep the same coupled power, the electron density in those plasma regions need to be higher which goes together with an increased temperature, see Fig. 4.

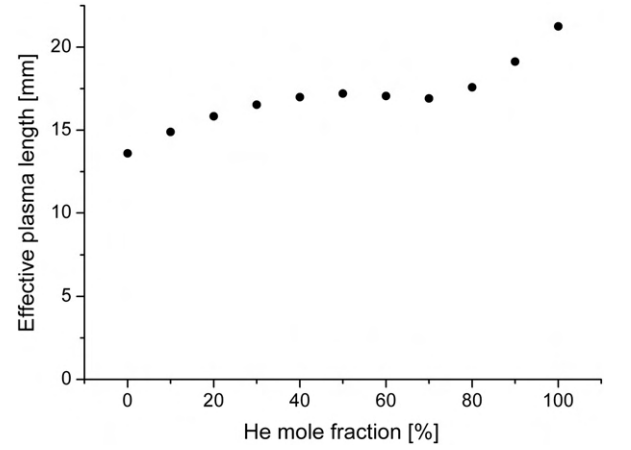

Fig. 8. Effective plasma length between the position where the temperature reaches 3000 K and a detection position at 10 mm above the load coil.

4.4. Pathlines of the central gas

For the detection of the analyte it is of high importance that it reaches the point of detection. In Fig. 10 several pathlines of the central gas are shown for different He fractions. As can be seen in Fig. 10a for the case of 60% He, all the pathlines are rather straight through the plasma. This applies also for all analysed conditions with lower helium content in the central gas. For a helium content of 70% (Fig. 10b), the outer pathlines widen somewhat but still go rather straight through the plasma. This is similar but becomes somewhat more pronounced for 80% helium. At a helium content of 90%, the pathlines have significantly changed, see Fig. 10c. Indeed, all the pathlines deviate from the straight path and run through the plasma at outer regions of the plasma. The same applies for a helium content of 100%, where this effect is even more pronounced; indeed some outer pathlines even run backwards in the torch (Fig. 10d). The white regions in the center of the pathlines for 90 and 100% He contain eddy structures. These positions are just not reached by the displayed pathlines. We believe that the behaviour of the pathlines originates from a competition of the dynamic force of the central gas stream and the viscous force of the plasma.

Thus, for up to about 70%, maybe 80%, of helium mole fraction in the central gas, a good transport of analyte takes place. However, if the helium content is increased further, it becomes worse. The droplets or particles will start to evaporate in the outer regions of the plasma. Hence, free analyte atoms will be produced there. These will then diffuse in the plasma, i.e. they will change the trajectory through the plasma, and will not be detected. For the lower helium contents, diffusion will take place, too, but it is less critical there. The analyte will distribute on a smaller cross-section and the main path will also be rather straight through the plasma, where it reaches the detection position, eventually.

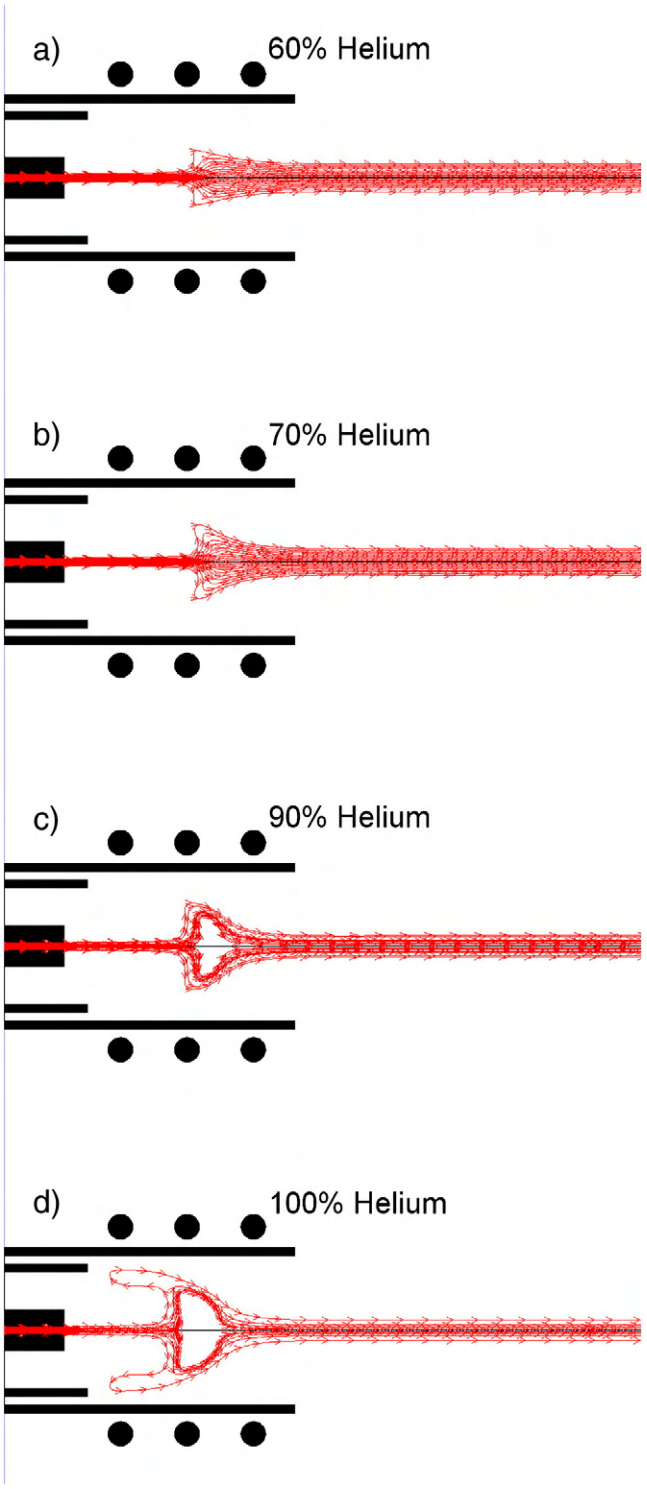

Fig. 10. Pathlines of the central gas for helium contents of a) 60%, b) 70%, c) 90% and d) 100% (mole fractions).

4.5. Helium distribution

In Fig. 11, the helium mole fraction distribution is shown for a helium content in the central gas of 50% and 100% together with the temperature of the plasma. For 50% helium, the central gas reaches a position where it is surrounded by the plasma, still containing a high fraction of the initial helium concentration. From there, the helium effectively starts to distribute towards outer regions. This is an important process since this improves the energy transfer from the outer part of the plasma towards the center. In the case of pure helium as central gas, helium already strongly distributes across the tube in

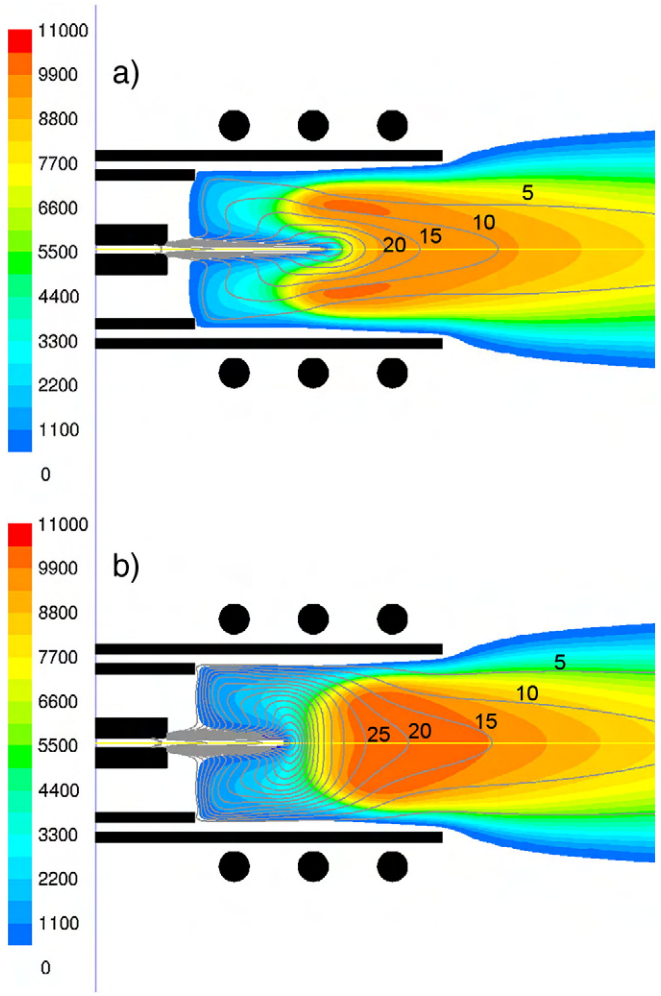

Fig. 11. The Helium mole fraction distribution for a) 50% He and 50% Ar and b) pure helium as central gas is displayed together with temperature distribution. The helium mole fractions are denoted by the numbers next to the dark line; unannotated lines denote changed helium mole fractions in steps of 5%. The temperature distribution (in K) is displayed by the colored contour plot.

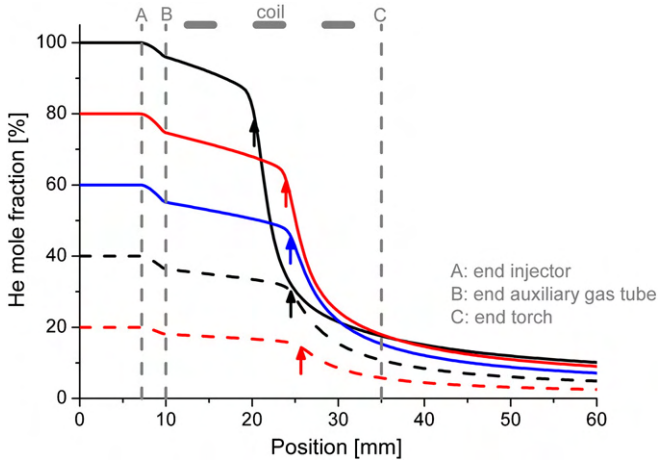

Fig. 12. Helium mole fractions along the axis. The initial helium mole fraction of the central gas for the respective curve is given by the value at the 0 mm-position. The arrows denote the positions where a temperature of 3000 K is reached.

front of the hot plasma. The distribution across the torch diameter is strong in this case. This can be understood as a result of the flow leading away from the center of the torch as shown by the pathlines in Fig. 10d. The central gas is transported towards the outer regions of the torch where it then mixes with the other gases due to diffusion within a relatively large volume. As a consequence, even in the case of pure helium as central gas, the maximum helium content in the hottest plasma regions is only about 25%.

Fig. 12 shows the helium mole fraction along the axis. One can see that slight mixing starts directly behind the end of the injector tube as to be expected. When the gas passes the end of the auxiliary gas tube, mixing proceeds somewhat more slowly until the gas reaches the starting position of the plasma (the respective positions as defined above are denoted with arrows). There, the helium mole fraction reduces significantly. Inside the plasma, the temperature rises and the number density reduces. As a consequence, the diffusion coefficient (see Eq. (20)) rises up to a factor of about 200 as to be expected from $D_{max}/D_{min} \approx (T_{max}/T_{min})^{3/2} \approx (10000\text{K}/300\text{K})^{3/2}$ and mixing is more efficient.

4.6. Electron density

The electron density distribution inside the plasma is shown in Fig. 13. The shape of the electron distribution follows basically the shape of the temperature distribution (cf. Fig. 4) while regions of higher temperature can be seen more pronounced here. With increasing helium content in the central gas, the electron distribution is shifted significantly in the downstream direction. The length of high electron density shortens at the outer positions of the torch while it increases in the center. The maximum electron density increases by a factor of about two going from pure argon to pure helium as central gas.

The electrons nearly exclusively originate from singly charged argon ions for any helium content in the central gas. However, although nearly no helium ions are present in the plasma, helium still influences the ionisation. Helium atoms replace argon and consequently, less argon atoms can donate electrons. From ionisation point of view, this situation is the same as if the plasma was burning at reduced pressure in pure argon (assuming LTE). Thus, to get the same electron density as for pure argon, the temperature needs to be higher, depending on the local helium concentration.

5. Conclusions

A model was developed in which the transport parameters are calculated for arbitrary mixtures of atomic species. In the present study, six different species were taken into account, namely electrons, atomic and singly charged helium and atomic, singly and doubly charged argon. The calculated values for viscosity and thermal conductivity are found to be in good agreement with literature data in the relevant temperature range. The data were derived only from the data for the pure elements. For the mixtures, a simple approximation (see Eq. (14)) was used for neutral-neutral and neutral-charged collisions. Thus, the data may not be as exact as if calculated taking into account the specific interaction. Nevertheless, the relative deviation does not increase for mixtures compared to pure elements. Thus, the model is applicable with reasonable accuracy. The advantage of this model is that only atomic-radius-data of the pure elements are required and the calculation can be performed in a rather straight-forward manner.

The simulation results show a strong effect on the plasma if helium is added to the central gas flow. The plasma length in the center becomes longer and also the temperature in the center increases with increasing He/Ar fraction. This is in agreement with the experimental results in [37] where higher temperatures in the central part of the plasma were found after helium addition to the central gas.

Both effects, i.e. longer and hotter plasma in the center, will have significant effect on an analyte that is injected into the plasma. The higher temperature will typically increase the evaporation velocity

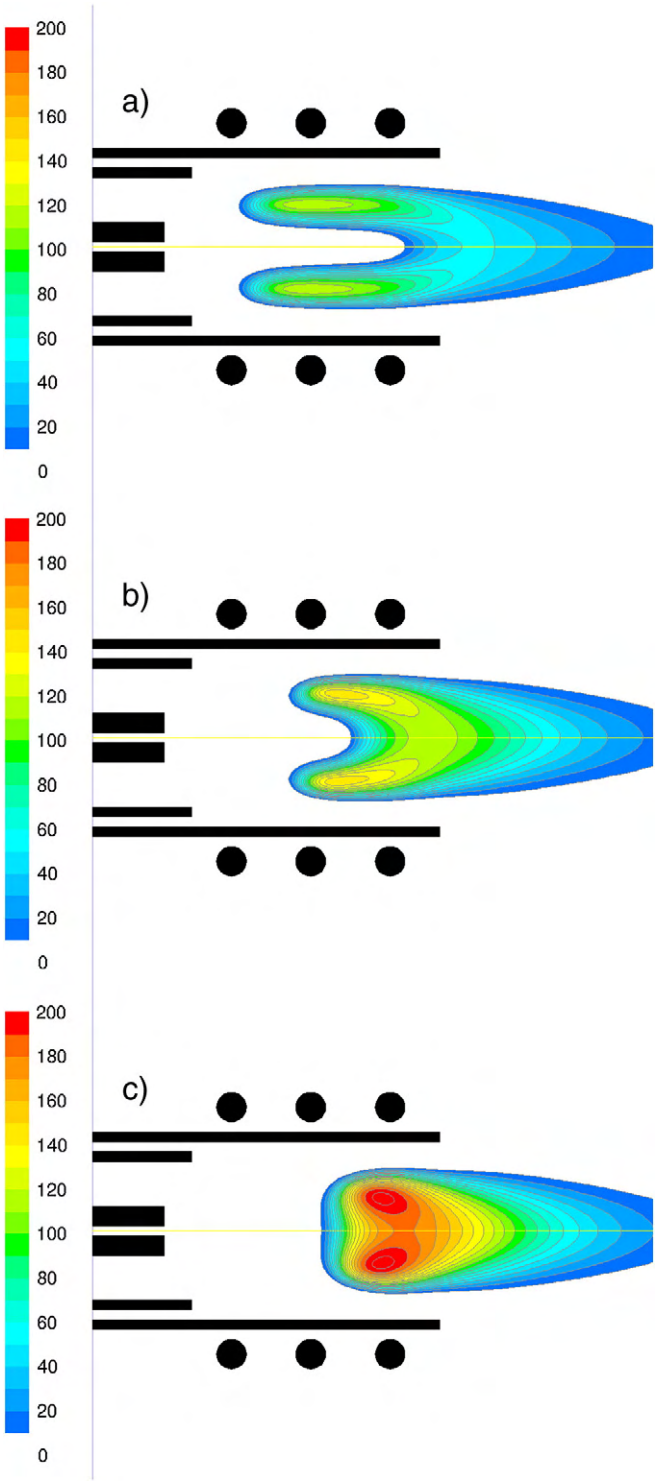

Fig. 13. Electron density distribution for helium mole fractions of a) 0%, b) 50% and c) 100% inside the central gas; the values are given in 10^{14} cm^{-3}. The lines are used to highlight the borders for the color levels in steps of $10 \cdot 10^{14}$ cm^{-3}. Note that for 100% Helium as central gas the maximum value reaches $204 \cdot 10^{14}$cm^{-3} and therefore the highest color level relates to two lines.

of droplets and particles. Additionally, the particles and droplets follow a longer path inside a hot region. This will also improve evaporation of the aerosol. Thus, larger particles and droplets can be evaporated completely using the helium addition. However, the gain might be not as large as presented for the conditions under study if optimum conditions are compared for pure argon and argon-helium-mixture, respectively. Indeed, the optimum conditions are dependent on the actual torch geometry and the actual instrument and were therefore not analysed in the present work. Nevertheless, an improvement of about one order of magnitude in sensitivity was found experimentally in laser ablation ICP-MS [38] using a helium/argon mixture as central gas. In this case, however, a significant part of the sensitivity gain has to be attributed also to improved laser ablation conditions using helium as background gas.

Note that the total volume flow rate through the central gas tube will be lower for optimum pure argon flow than for a mixed helium-argon flow at optimum conditions. Thus, the helium addition is advantageous if high volume gas flow rates through the central channel will be used. Such conditions are advantageous for instance for laser ablation spatial-mapping measurements. For this purpose, many laser pulses are applied and the individual signals need to be detected separately. A higher volume flow rate is (nearly) directly linked to a reduced washout time of the aerosol transport setup [38,39]. Thus, the measurement time can be reduced or the resolution can be improved using higher flow rates.

Due to its higher thermal conductivity, helium transports more energy towards the center of the plasma compared to the case of pure argon. Thus, a local cooling inside the center of the plasma can more easily be compensated. Such a cooling (at a fixed central gas flow rate) would usually originate from the evaporating droplets or particles injected into the plasma. This cooling effect can be stable in time (continuously injected droplets) but the temperature would be lower [40]. Thus, excitation and/or ionisation of the analyte would typically be lower than without droplets. The energy loss occurs in the central part of the plasma while the power coupling happens in the outer regions. Thus, heat conduction and not convection is the dominant process to transfer the energy to the center – which takes place more effectively if helium is added. Of course, also the constituents of the aerosol can improve the heat transfer. That, however, only happens after (a part of) the aerosol is already evaporated. Additionally, energy will be needed for ionisation and/or dissociation.

We expect that the optimum helium mole fraction will be in the range of about 40 to 70%. In that range, the amount of helium is already sufficiently high to have a significant effect. Moreover, the effect of the addition in this range on the temperature appears to be linear, whereas deviations from linearity are observed for He mole fraction of 80% or higher. Moreover, for higher He mole fractions the pathlines of the central gas deviate from a straight way through the plasma which is undesirable. However, these optimum conditions need to be verified experimentally.

It should be noted that the present discussion does not cover all important figures of merit for analytic performance such as detailed information of effects on detection limits or easy operation of the instrument. Such investigations, however, require direct experimental investigation. Nevertheless, we conclude that helium addition to the central gas stream improves the analytical performance of the ICP.

Acknowledgement

This work was financially supported by the IAP-P6/42 project "Quantum Effects in Clusters and Nanowires". The calculation support of the core facility CALCUA, provided by the University of Antwerp, is gratefully acknowledged.

Appendix A. List of symbols

Symbol	Description	Unit
B_{1r}	Magnetic field amplitude in radial direction, cosine time dependence	T
B_{1z}	Magnetic field amplitude in axial direction, cosine time dependence	T
B_{2r}	Magnetic field amplitude in radial direction, sine time dependence	T
B_{2z}	Magnetic field amplitude in axial direction, sine time dependence	T
b_0	90-degree collision parameter	m
c_p	Specific heat capacity at constant pressure	J/(kg K)
d	diameter	m
$E_{1\phi}$	Electric field amplitude in angular direction, cosine time dependence	V/m
$E_{2\phi}$	Electric field amplitude in angular direction, sine time dependence	V/m
E_{ion}	Ionisation potential	J
ΔE_{ion}	Ionisation potential reduction	J
e	Elementary charge	C
f	Force density	N/m^3
H	Enthalpy	J/kg
h	Planck constant	J s
j	Electric current density	A/m^2
j_{ext}	Electric current density inside the coil	A/m^2
K_{kZ}	Right hand side of Saha-equation for species k and ionisation stage Z	m^{-3}
k	Thermal conductivity	W/(m K)
k_B	Boltzmann constant	J/K
M	Molar mass	kg/mol
m_e	Electron mass	kg
m_k	Atomic mass of species k	kg
N_A	Avogadro constant	1/mol
n_{Hges}	Total number density of heavy species	m^{-3}
n_e	Electron number density	m^{-3}
$n_{k,\,Z}$	Heavy particle number density of species k and in the ionisation stage Z	m^{-3}
p	Power density	J/m^3
$R_{eff,\,k}$	Effective atomic radius	m
r	Radial coordinate	m
S_{ki}	Collision cross-section for species k and species i	m^2
T	Temperature	K
t	Time	s
x	Number density fractions	–
Z	Charge number	–
Z_{av}	Average charge number	–
$ln\Lambda_C$	Coulomb logarithm	–
λ_B	de Broglie length	m
λ_D	Debye-length	m
ε_0	Dielectric constant	C/(V m)
μ_0	Magnetic permeability	V s/(A m)
μ_{ki}	Reduced mass for species k and species i	kg
η	Dynamic viscosity	Pa s
σ	Electric conductivity	S/m
$\zeta_{k,\,Z}$	Partition function of species k and in the ionisation stage Z	–
ω	Circular frequency	1/s

References

[1] R.S. Houk, V.A. Fassel, G.D. Flesch, H.J. Svec, Inductively coupled argon plasma as an ion source for mass spectrometric determination of trace elements, Anal. Chem. 52 (1980) 2283–2289.
[2] P.W.J.M. Boumans, F.J. de Boer, Studies of flame and plasma torch emission for simultaneous multi-element analysis — I Preliminary investigations, Spectrochim. Acta B 27 (1972) 391–414.
[3] V.A. Fassel, R.N. Kniseley Test, Inductively coupled plasma. Optical emission spectroscopy, Anal. Chem. 46 (1974) 1110A–1120A.
[4] C.C. Garcia, A. Murtazin, S. Groh, V. Horvatic, K. Niemax, Characterization of single Au and SiO_2 nano- and microparticles by ICP-OES using monodisperse droplets of standard solutions for calibration, J. Anal. At. Spectrom. 25 (2010) 645–653.
[5] S. Groh, P.K. Diwakar, C.C. Garcia, A. Murtazin, D.W. Hahn, K. Niemax, 100% efficient sub-nanoliter sample introduction in laser-induced breakdown spectroscopy and inductively coupled plasma spectrometry: implications for ultralow sample volumes, Anal. Chem. 82 (2010) 2568–2573.

[6] J.N. Schaper, J.H. Petersen, J. Maßmann, N.H. Bings, Potential of a novel low-flow drop-on-demand aerosol generator for plasma spectrochemical and speciation analysis, Poster, 37th FACSS Conference, Raleigh, USA, 2010.
[7] H. Yabuta, H. Miyahara, M. Watanabe, E. Hotta, A. Okino, Design and evaluation of dual inlet ICP torch for low gas consumption, J. Anal. At. Spectrom. 17 (2002) 1090–1095.
[8] A. Klostermeier, C. Engelhard, S. Evers, M. Sperling, W. Buscher, New torch design for inductively coupled plasma optical emission spectrometry with minimized gas consumption, J. Anal. At. Spectrom. 20 (2005) 308–314.
[9] A. Scheffer, R. Brandt, C. Engelhard, S. Evers, N. Jakubowski, W. Buscher, A new ion source design for inductively coupled plasma mass spectrometry (ICP-MS), J. Anal. At. Spectrom. 21 (2006) 197–200.
[10] G.C.-Y. Chan, G.M. Hieftje, Use of vertically resolved plasma emission as an indicator for flagging matrix effects and system drift in inductively coupled plasma-atomic emission spectrometry, J. Anal. At. Spectrom. 23 (2008) 193–204.
[11] F. Vanhaecke, R. Dams, C. Vandecasteele, 'Zone model' as an explanation for signal behaviour and non-spectral interferences in inductively coupled plasma mass spectrometry, J. Anal. At. Spectrom. 8 (1993) 433–438.
[12] D. Bernardi, V. Colombo, E. Ghedini, A. Mentrelli, Three-dimensional modelling of inductively coupled plasma torches, Eur. Phys. J. D 22 (2003) 119–125.
[13] M. Cai, A. Montaser, J. Mostaghimi, Computer simulation of atmospheric-pressure helium inductively coupled plasma discharges, Spectrochim. Acta Part B 48 (1993) 789–807.
[14] R.M. Barnes, S. Nikdel, Temperature and velocity profiles and energy balances for an inductively coupled plasma discharge in nitrogen, J. Appl. Phys. 47 (1976) 3929–3934.
[15] S.L. Girshick, W. Yu, Radio-frequency induction plasmas at atmospheric pressure: mixtures of hydrogen, nitrogen, and oxygen with argon, Plasma Chem. Plasma Proc. 10 (1990) 515–529.
[16] M. Cai, D.A. Haydar, A. Montaser, J. Mostaghimi, Computer simulation of argon–nitrogen and argon-oxygen inductively coupled plasmas, Spectrochim. Acta Part B 52 (1997) 369–386.
[17] S.B. Punjabi, T.K. Das, N.K. Joshi, H.A. Mangalvedekar, B.K. Lande, A.K. Das, The effect of various coil parameters on ICP torch simulation, J. Phys. Conf. Ser. 208 (2010) 012048.
[18] S. Xue, P. Proulx, M.I. Boulos, Extended-field electromagnetic model for inductively coupled plasma, J. Phys. D Appl. Phys. 34 (2001) 1897–1906.
[19] Y. Tanaka, Two-temperature chemically non-equilibrium modelling of high-power Ar–N_2 inductively coupled plasmas at atmospheric pressure, J. Phys. D Appl. Phys. 37 (2004) 1190–1205.
[20] Y. Tanaka, Time-dependent two-temperature chemically non-equilibrium modelling of high-power Ar–N_2 pulse-modulated inductively coupled plasmas at atmospheric pressure, J. Phys. D Appl. Phys. 39 (2006) 307–319.
[21] P. Yang, J.A. Horner, N.N. Sesi, G.M. Hieftje, Comparison of simulated and experimental fundamental ICP parameters, Spectrochim. Acta Part B 55 (2000) 1833–1845.
[22] ANSYS FLUENT 12.0/12.1 Documentation.
[23] A. Montaser, D.W. Golightly, Inductively coupled plasmas in analytical atomic spectrometry", 2nd edition, VCH Publishers, 1992.
[24] A.T.M. Wilbers, J.J. Beulens, D.C. Schram, Radiative energy loss in a two-temperature argon plasma, J. Quant. Spectrosc. Radiat. Transfer 46 (1991) 385–392.
[25] G.J. Bastiaans, R.A. Mangold, The calculation of electron density and temperature in Ar spectroscopic plasmas from continuum and line spectra, Spectrochim. Acta Part B 40 (1985) 885–892.
[26] D. Bernardi, V. Colombo, E. Ghedini, A. Mentrelli, Comparison of different techniques for the FLUENT-based treatment of the electromagnetic field in inductively coupled plasma torches, Eur. Phys. J. D 27 (2003) 55–72.
[27] D'Ans, Lax, "Taschenbuch für Chemiker und Physiker, Band 1; Physikalisch-chemische Daten", 4th edition, Springer-Verlag, 1992.
[28] A.B. Murphy, C.J. Arundell, Transport coefficients of argon, nitrogen, oxygen, argon-nitrogen, and argon-oxygen plasmas, Plasma chem. plasma proc. 14 (4) (1994) 451–490.
[29] A.B. Murphy, Transport coefficients of helium and argon–helium plasmas, IEEE Transact. Plasma Sci. 25 (1997) 809–814.
[30] Bergmann, Schaefer, "Band 5: Vielteilchenphysik", Walter de Gruyter Berlin, New York, 1992.
[31] J.O. Hirschfelder, C.F. Curtis, R.B. Bird, Molecular Theory of Gases And Liquids, 4th edition, John Wiley & Sons, 1967.
[32] W.L.T. Chen, J. Heberlein, E. Pfender, B. Pateyron, G. Delluc, M.F. Elchinger, Thermodynamic and transport properties of Argon/Helium plasmas at atmospheric pressure, Plasma Chem. Plasma Proc. 15 (3) (1995) 559–579.
[33] J.D. Ramshaw, C.H. Chang, Ambipolar diffusion in multicomponent plasmas, Plasma Chem. Plasma Proc. 11 (1991) 395.
[34] M.R. Zaghloul, M.A. Bourham, J.M. Doster, A simple formulation and solution strategy of the Saha equation for ideal and nonideal plasmas, J. Phys. D Appl. Phys 33 (2000) 977–984.
[35] M.R. Zaghloul, Reduced formulation and efficient algorithm for the determination of equilibrium composition and partition functions of ideal and nonideal complex plasma mixtures, Phys. Rev. E 69 (2004) 026702.
[36] A.W. Irwin, Polynomial partition function approximations of 344 atomic and molecular species, Astrophys. J. Suppl. Series 45 (1981) 621–633.
[37] P. Heitland, J.A.C. Broekaert, Addition of small amounts of helium and hydrogen to the working gases in slurry nebulization inductively coupled plasma atomic emission spectrometry for the analysis of ceramic powders, J. Anal. At. Spectrom. 12 (1997) 981–986.
[38] D. Günther, C.A. Heinrich, Enhanced sensitivity in laser ablation-ICP mass spectrometry using helium-argon mixtures as aerosol carrier, J. Anal. At. Spectrom. 14 (1999) 1363–1368.
[39] H. Lindner, D. Autrique, C.C. Garcia, K. Niemax, A. Bogaerts, Optimized transport setup for high repetition rate pulse-separated analysis in laser ablation-inductively coupled plasma mass spectrometry, Anal. Chem. 81 (2009) 4241–4248.
[40] M. Huang, D.S. Hanselman, P. Yang, G.M. Hieftje, Isocontour maps of electron temperature electron number density and gas kinetic temperature in the Ar inductively coupled plasma obtained by laser-light Thomson and Raleigh scattering, Spectrochim. Acta Part B 47 (1992) 765–785.